



Analyzing Surface Ruggedness Inside and Outside of Ice Stability Zones at the Lunar Poles

Ariel N. Deutsch¹ , Jennifer L. Heldmann¹, Anthony Colaprete¹, Kevin M. Cannon^{2,3}, and Richard C. Elphic¹

¹NASA Ames Research Center, Mountain View, CA 94035, USA; ariel.deutsch@nasa.gov

²Colorado School of Mines, Department of Geology and Geological Engineering, Golden, CO 80401, USA

³Colorado School of Mines, Space Resources Program, Golden, CO 80401, USA

Received 2021 April 24; revised 2021 August 6; accepted 2021 September 7; published 2021 October 14

Abstract

We measured surface ruggedness within 12 polar craters on the Moon, six at each pole, using a variation of the Vector Ruggedness Measure (VRM*). We compare VRM* values derived within ice stability zones, where maximum surface temperatures are ≤ 112 K, to VRM* values from warmer surfaces where ice is not stable. Ruggedness values inside and outside of ice stability zones are statistically not from the same continuous distribution ($\alpha = 0.05$). In nine of the 12 investigated craters, surfaces where ice is stable are smoother than neighboring warmer surfaces. These comparatively smooth surfaces are observed in both craters that host surface water-ice exposures and those that do not, suggesting that the presence of subsurface ice, rather than surface ice, may be responsible for the reduced surface ruggedness derived from a moving window of 3×3 cells applied to 120 m elevation models. Reduced ruggedness of ice stability zones is slightly greater in south polar craters and tends to correlate with enhanced hydrogen content as modeled from Lunar Prospector data. While ice stability zones may have a control on the distribution of softened topography at the lunar poles, the magnitude of this softening is small at the investigated baselines.

Unified Astronomy Thesaurus concepts: The Moon (1692); Lunar science (972); Planetary polar regions (1251); Surface processes (2116); Planetary surfaces (2113); Surface ices (2117); Surface variability (2114)

1. Introduction

The lunar poles are a high-priority science target owing to the enhanced presence of volatiles (Watson et al. 1961; Arnold 1979; Feldman et al. 1998; Colaprete et al. 2010; Lucey et al. 2014; Hayne et al. 2015; Fisher et al. 2017; Li et al. 2018; Rubanenko et al. 2019; Hayne et al. 2020). The low obliquity of the Moon helps maintain extremely low polar temperatures, which allow for the cold trapping of ices beneath and even at the surface (Vasavada et al. 1999; Paige et al. 2010; Mazarico et al. 2011; Schorghofer & Aharonson 2014; Kloos et al. 2019). Of interest to both the science and exploration communities, water ice (H_2O) can survive for geologic timescales without sublimating in regions where temperatures are ≤ 112 K (Watson et al. 1961; Vasavada et al. 1999; Paige et al. 2010), referred to here as ice stability zones (ISZs).

Today, many questions still exist about the nature of ice contained in ISZs, including the distribution (both areal and vertical), physical form, and abundance of ice. Some observations are suggestive of thin transient frosts or well-mixed icy regolith directly at the surface of some, but not all, ISZs (Haruyama et al. 2008; Hayne et al. 2015; Fisher et al. 2017; Li et al. 2018; Farrell et al. 2019), and the spatial heterogeneity of these observations varies within individual ISZs (Deutsch et al. 2020a). Other data are suggestive of diffuse ices present within the shallow subsurface and are not suggestive of thick accumulations of near-surface ice deposits (Campbell et al. 2006; Colaprete et al. 2010; Feldman et al. 2001; Lawrence et al. 2006; Thomson et al. 2012). Yet other data indicate a shallowing of polar craters with latitude, interpreted to be due

to the presence of many-meters-thick icy regolith deposits in the subsurface (Kokhanov et al. 2015; Rubanenko et al. 2019). Such thick ice-bearing layers, which appear to influence crater morphometry (Kokhanov et al. 2015; Rubanenko et al. 2019), could also influence the texture of the overlying surfaces. Thus, characterizing surface textures on the Moon could reveal important information about how lunar ice is distributed.

Understanding surface texture is also important for future ground-based exploration efforts. Naturally, the exciting discoveries of lunar volatiles have generated more interest in exploring the Moon—interest founded in both science and in situ resource utilization. Characterizing surface texture is directly applicable to characterizing surface traversability and hazards (De Rosa et al. 2012; Heldmann et al. 2016), an essential component in planning for future successful robotic (e.g., Ivanov et al. 2015; Colaprete et al. 2020; Ohtake et al. 2020) and eventually human surface operations.

Here we characterize surface texture at 20–120 m scales by measuring the surface ruggedness within 12 polar craters (six at each pole). We analyze the relationship between surface ruggedness and surface temperature and discuss the possibility that polar ice is softening surface topography within ISZs.

2. Methods

2.1. Surface Ruggedness Indices

We analyzed the surface texture of 12 craters that were selected on the basis of (1) location (the craters are centered between 80° and 90° at either pole), (2) illumination conditions (the floors of the craters have a distinct boundary between an ISZ and a non-ISZ), and (3) size (the craters are large enough such that a flat ($<10^\circ$ slope at 20 m scales) floor that includes both an ISZ and non-ISZ could be analyzed). We analyzed only portions of craters' floors with slopes $<10^\circ$ because texture



Original content from this work may be used under the terms of the [Creative Commons Attribution 4.0 licence](https://creativecommons.org/licenses/by/4.0/). Any further distribution of this work must maintain attribution to the author(s) and the title of the work, journal citation and DOI.

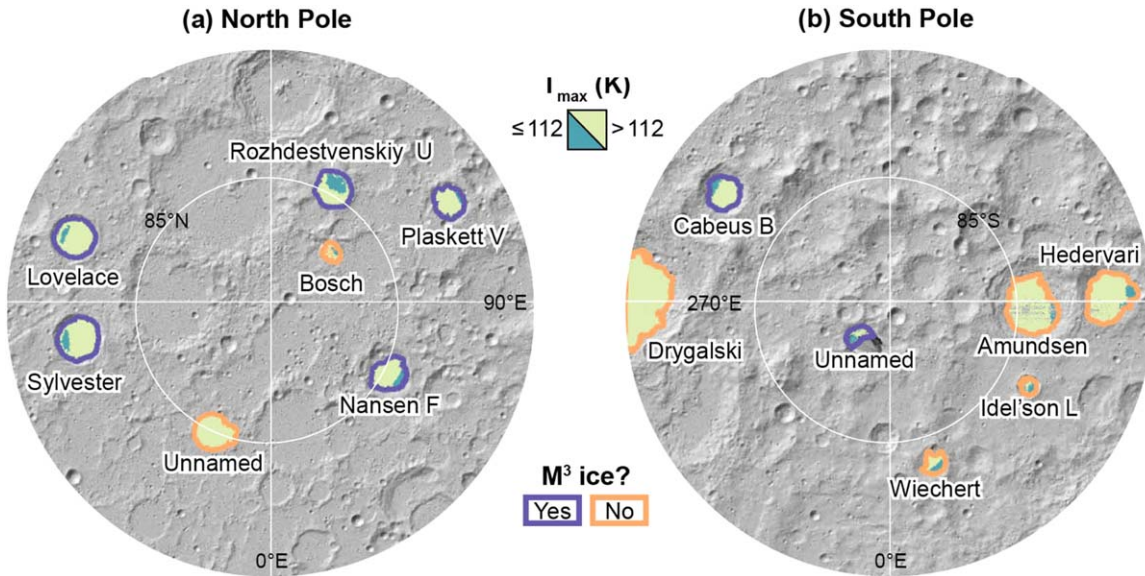


Figure 1. Craters analyzed in this study superposed on LOLA hillshade maps. The coloring within each crater designates regions where maximum surface temperatures are ≤ 112 K (blue) and > 112 K (green) during (a) northern and (b) southern summer (Williams et al. 2019). The outlines of craters follow topography contours and are colored to designate whether surface water-ice exposures have (blue) or have not (orange) been detected (Li et al. 2018).

measurements can be correlated with slope (Sappington et al. 2007). We selected six craters in the north polar region (Bosch, Lovelace, Nansen F, Plaskett V, Rozhdestvenskiy U, and Sylvester) and six craters in the south polar region (Amundsen, Cabeus B, Hedervari, Idel'son L, an unnamed one, and Wiechert) that met these selection criteria in order to build a suitable statistical representation of polar craters (Figure 1). We also analyzed two craters whose maximum surface temperatures do not fall below 112 K for standards of comparison: an unnamed crater in the north (84.9°N , 26.5°E), and Drygalski in the south (Figure 1). Note that other craters fit these criteria and the study could be expanded to other locations in the future.

We measured surface ruggedness with the vector ruggedness measure (VRM) using the Arc Hydro toolbox in ArcGIS. The VRM expresses ruggedness as the dispersion of vectors normal to planar facets on a surface (Hobson 1972; Sappington et al. 2007). As explained in detail by Sappington et al. (2007), first the slope (α) and aspect (β) of each cell are calculated using a 3×3 moving window by fitting a plane to the nine local cells in the window. Unit vectors normal to each digital elevation model (DEM) cell are next decomposed into their x , y , and z components using standard trigonometry, and α and β of each cell:

$$\begin{aligned} z &= 1 \times \cos(\alpha) \\ xy &= 1 \times \sin(\alpha) \\ x &= xy \times \sin(\beta) \\ y &= xy \times \cos(\beta). \end{aligned}$$

Then, a moving window is used to calculate the magnitude of the resultant vector, $|r|$, centered on each DEM pixel by summing up the x , y , and z components for a window of 3×3 pixels:

$$|r| = \sqrt{(\sum x)^2 + (\sum y)^2 + (\sum z)^2}.$$

Finally, a dimensionless ruggedness value is calculated by subtracting the magnitude of the resultant vector in standardized

form from 1:

$$\text{VRM} = 1 - \frac{|r|}{n},$$

where n is the number of cells in the window. All of these values were calculated through the ArcGIS Vector Ruggedness Metric tool (Sappington et al. 2007). VRM is a unitless measurement, ranging from 0 (no terrain variation) to 1 (complete terrain variation). To translate VRM into a more intuitive metric, we calculated VRM^* in degrees, representing the characteristic angle of surface normal variation:

$$\text{VRM}^* = \sqrt{2 \times \text{VRM}} \frac{180^\circ}{\pi \text{ radians}}.$$

Because slope and aspect are decomposed into three-dimensional vector components, the VRM^* is decoupled from surface slope and elevation, which is a benefit of the VRM^* over other common ruggedness indices (Hobson 1972; Sappington et al. 2007; Amatulli et al. 2018). A major strength of the VRM^* is that it can distinguish between a highly rugged terrain and a steep, even terrain (Figure 2; Sappington et al. 2007).

Calculating VRMs requires a topography input, and we used LOLA-derived DEMs at pixel resolutions of 120, 40, and 20 m, as well as 10 m where available ($\geq 85^\circ$) (https://pds-geosciences.wustl.edu/lro/lro-l-lola-3-rdr-v1/lrolol_1xxx/data/lola_gdr/polar/). While 10 mpp DEMs offer the highest spatial resolution, they are associated with greater uncertainty in slope measurements because the absolute error in height remains the same as the baseline over which the slope is measured is reduced (Barker et al. 2020); the LOLA vertical uncertainty of ~ 1 m creates $\sim 10\%$ uncertainty in slopes measured from a 10 mpp DEM. Furthermore, higher spatial resolution DEMs often rely on more interpolation because there are fewer laser shots for each grid cell (Table 1). Therefore, we choose to report our statistics from measurements derived from 120 mpp DEMs, so that the majority of pixels for which we derive ruggedness parameters have LOLA elevation measurements, rather than

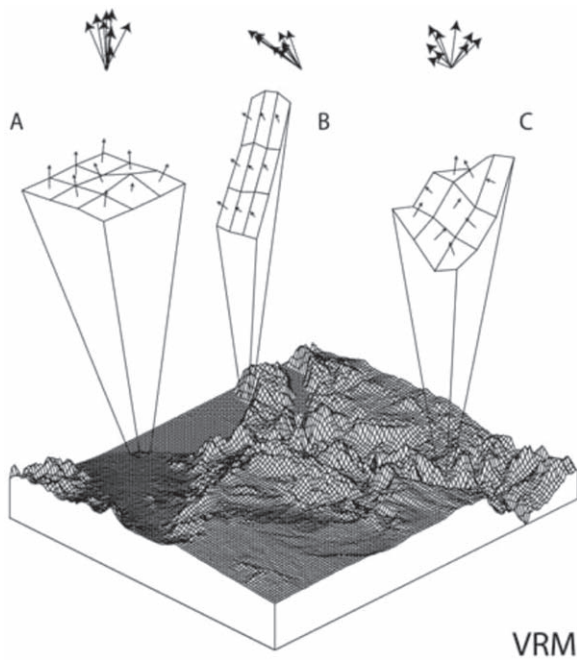


Figure 2. Graphical depiction of a VRM calculation from Sappington et al. (2007). VRMs are low for (a) flat surfaces and (b) steep, even surfaces, but high for (c) steep, rugged surfaces.

Table 1

Percentage of Study Surface Areas That Are Covered by LOLA Shots for 120, 40, and 20 mpp DEMs

Location	DEM Resolution (mpp)		
	120	40	20
Region or crater name			
South polar region (80°–90°S)	94.98	64.24	33.09
Amundsen	98.18	65.73	29.31
Cabeus B	96.61	64.39	31.72
Hedervari	93.26	52.89	22.45
Idel'son L	99.01	73.55	36.26
Unnamed	100.00	95.47	64.47
Wiechert	99.01	70.85	33.34
North polar region (80°–90°N)	72.49	35.57	15.53
Bosch	99.70	78.06	40.42
Lovelace	69.87	28.40	11.66
Nansen F	86.99	45.11	18.48
Plaskett V	73.94	34.68	13.79
Rozhdestvenskiy U	91.30	49.94	21.17
Sylvester	62.67	26.47	10.54

interpolated elevation estimates. Because surface texture is wavelength dependent, comparing VRM* values derived from DEMs or windows of different spatial resolutions is not appropriate.

In order to interpret texture indices meaningfully, we only compared those on a crater-by-crater basis; therefore, texture indices derived for individual craters are not compared to those

derived for other craters. This is because the texture of a planetary surface is influenced by its age (i.e., exposure time to impact processes), as well as its composition (i.e., material properties), as well as the presence of rocks and boulders; Kreslavsky & Head 2000, 2002; Rosenburg et al. 2011; Kreslavsky et al. 2013; Jawin et al. 2014; Neumann et al. 2015; Wang et al. 2020; Deutsch et al. 2020b). Kreslavsky et al. (2013) showed that on the Moon hectometer-scale roughness appears to be controlled by regolith formation and modification processes, while kilometer-scale roughness appears to be controlled by bedrock geology and major geologic events, such as impacts, volcanism, or tectonism.

2.2. Surface Thermal Environment

We analyzed the thermal environment at each study site using the average (T_{avg}) and maximum (T_{max}) surface temperatures, measured for north and south polar local summer by the Diviner Lunar Radiometer Experiment (Williams et al. 2019). Thus, T_{max} represents the maximum temperatures experienced at the surface throughout the seasonal cycles of the Moon (defined by the times of year when the subsolar latitude is above or below the equator), providing the largest constraint on present-day surface ice stability. These surface temperatures were presented by Williams et al. (2019) and are available online (<http://luna1.diviner.ucla.edu/~jpierre/diviner>).

3. Results

3.1. Surface Thermal Environment

The VRM* measurements at 120, 40, and 20 mpp DEMs reveal a bimodal distribution with respect to maximum surface temperature (Figures 3–6) for each of the 12 analyzed craters. The individual modes are much more distinctive in T_{max} space than they are in T_{avg} space (Figures 2 and 3) and often not resolvable in T_{avg} space. The modes are defined by the T_{max} values corresponding to local maximum count densities. The location of Mode 1 is associated with surfaces where ice is stable, generally centered around $T_{\text{max}} \sim 95$ K (mean = 96 K, median = 97 K, range = [59 K, 108 K]), determined by the temperature with the highest pixel count number. Of the 12 craters analyzed, the only anomaly to this observation is with Amundsen, whose first mode centers around T_{max} of ~ 65 K (Figure 4).

Mode 2 represents the distribution of temperatures for an illuminated polar surface. For example, a crater whose maximum surface temperature does not fall below 112 K has a unimodal distribution of VRM*s in T_{max} space (Figure 5). Mode 1 is unique to polar craters that host ISZs ($T_{\text{max}} \leq 112$ K). The location of Mode 2 is much more variable than the location of Mode 1, reflective of each crater's individual thermal environment, but is generally centered at T_{max} between 170 and 235 K.

The same patterns between texture indices and temperature are resolvable at pixel resolutions of 10, 20, 40, and 120 m (Figure 6). VRM*s derived from higher-resolution DEMs are also more sensitive to local variations, and the derived aspect and slope components used to calculate VRM*s have higher variability at high spatial resolutions (Amatulli et al. 2018). This results in greater variability in VRM* values derived for a local scene at higher spatial resolution. The VRMs derived at each investigated spatial resolution are archived and available for use Zenodo: doi:10.5281/zenodo.4716357.

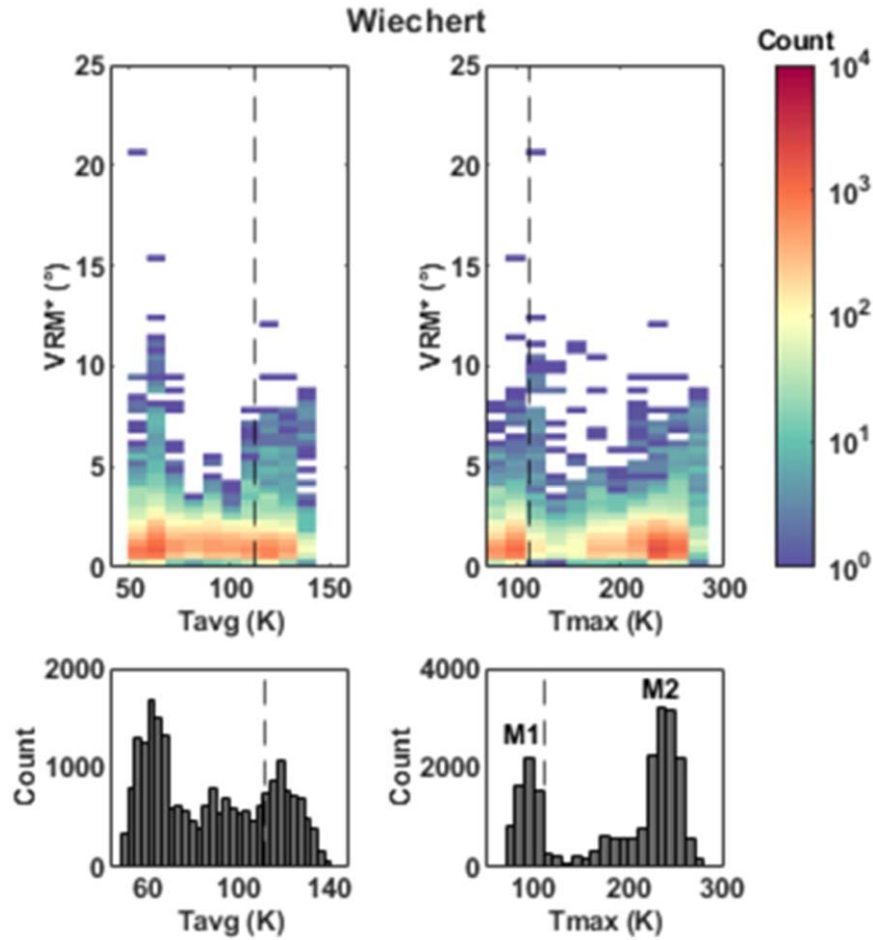


Figure 3. Top: binned scatter plots display the relationships between VRM* and surface temperature for Wiechert (85.2°S, 182.4°E) with counts plotted on a log scale. The dashed vertical line in each panel occurs at $T = 112$ K. The VRM*s were derived at a pixel resolution of 120 m, and surface temperatures were upsampled to the same resolution using bilinear interpolation. Bottom: histograms show the distribution of temperature values. Modes 1 and 2 are labeled as M1 and M2 in T_{\max} space.

3.2. The Magnitude of Topographic Ruggedness

VRM*s provide information about the magnitude of terrain ruggedness, representing the characteristic angle in degrees of surface normal variations at the scale of the moving window. In Table 2, we report statistics on VRM*s for ISZs and non-ISZs within each analyzed crater, derived from 3×3 windows of 120 mpp DEMs.

Two-sample Kolmogorov–Smirnov tests indicate that the ruggedness within ISZs and that outside of ISZs are not from the same continuous distribution ($\alpha = 0.05$). ISZs are smoother than neighboring warmer surfaces, where ice is not stable, for nine of the 12 investigated craters. The mean and median VRM*s inside these nine ISZs are ~ 0.17 – 0.18 smaller than those in the non-ISZs, derived from 120 mpp DEMs using a moving window size of three cells, although this difference is smaller than the standard deviation (SD) of each population. The three craters whose ISZs are not smoother are Lovelace (median only) and Bosch in the north and an unnamed crater in the south. Perhaps the ISZs of these three craters are influenced by rougher initial topography. For example, if the ISZ happens to have more superposing craters, it will have enhanced surface ruggedness (Kreslavsky & Head 2000, 2002; Rosenberg et al. 2011; Kreslavsky et al. 2013; Jawin et al. 2014; Neumann et al. 2015; Wang et al. 2020; Deutsch et al. 2020b).

For each of the 12 investigated craters, there is substantial scatter in the data (e.g., Figures 2–4), and the VRM*s of ISZ

and non-ISZ populations overlap for each crater (Table 2). Frequency histograms of VRM*s illustrate the large overlap of values between surfaces where water ice is and is not stable (Figure 7), highlighting that there are surfaces outside of ISZs that are just as smooth as those inside ISZs at the investigated spatial scales (Figures 8, 9).

The scatter in our measurements of ruggedness may stem from the natural topographic variations across the landscape (e.g., the distribution of impact craters) or from uncertainties associated with the LOLA gridded data (Barker et al. 2020). To assess whether the ruggedness differences inside and outside ISZs are an artifact of natural topographic variability, we measured ruggedness in six adjacent regions located outside of Amundsen’s ISZ (Figure 10). The set of median ruggedness values (Table 3) represents the natural variability of the median ruggedness outside the ISZ of Amundsen. The median VRM* inside Amundsen’s ISZ (1.10) is outside the range of these non-ISZ medians (1.80 – 2.58), suggesting that the difference between ISZ and non-ISZ ruggedness is meaningful.

Amundsen crater has one of the most subdued ISZs in comparison to its non-ISZ, with mean and median VRM*s that are 0.43 and 0.37 less than those for its non-ISZ. However, these differences are not larger than the SD of the derived VRM*s (Table 2). Idel’son L and Cabeus B also show enhanced softening (VRM*s are ~ 0.30 lower in their ISZs compared to ~ 0.18 for the whole study group). The craters

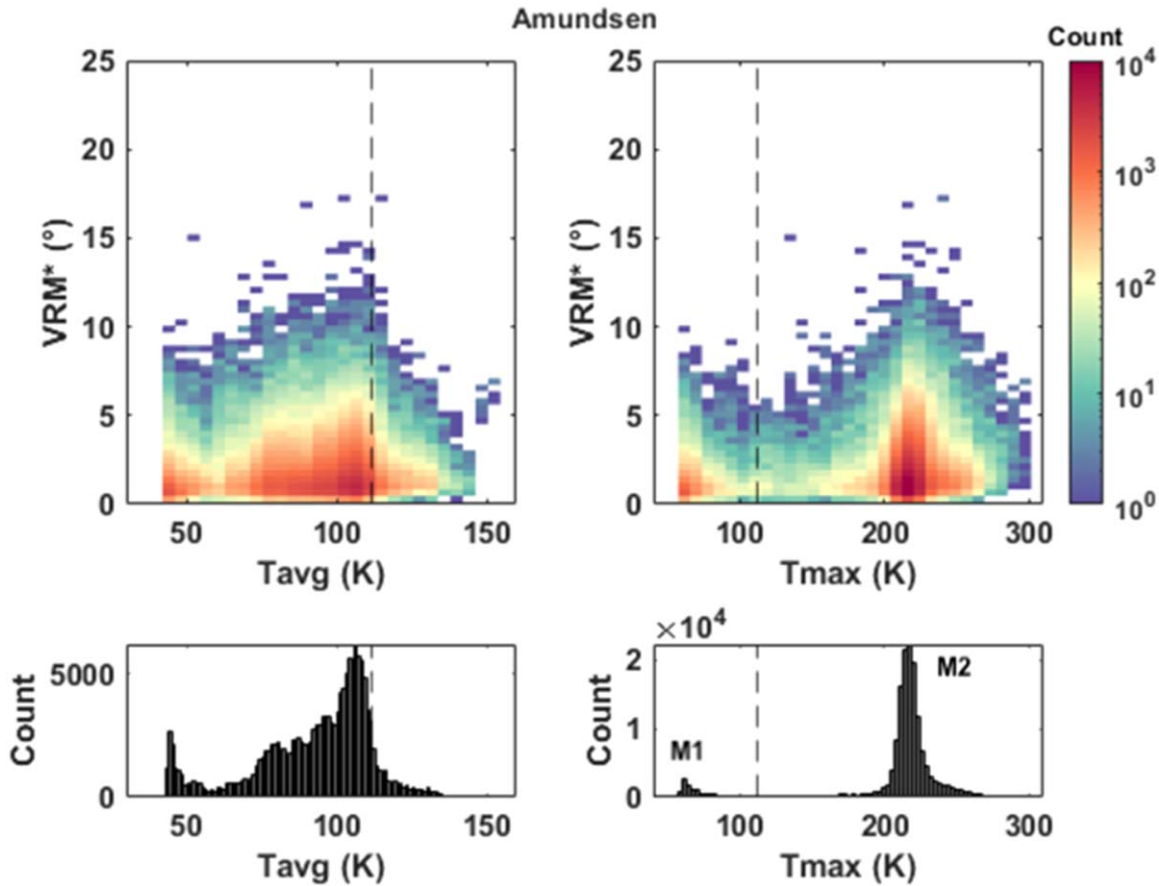


Figure 4. Top: binned scatter plots (with counts on a log scale) display the relationships between VRM^* s and surface temperature for Amundsen (84.4°S, 83.1°E) at a pixel resolution of 120 m. The dashed vertical line in each panel occurs at $T = 112$ K. The VRM^* s were derived at a pixel resolution of 120 m, and surface temperatures were upsampled to the same resolution using bilinear interpolation. Bottom: histograms show the distribution of temperature values. Modes 1 and 2 are labeled as M1 and M2 in T_{max} space. Amundsen is unique in that its Mode 1 is centered at a lower temperature than the other 11 investigated craters.

with the highest amount of ISZ softening do not have drastically different thermal environments than those of the other investigated craters (Williams et al. 2019), and they are estimated to be of similar ages to the other craters in our study set (Tye et al. 2015; Cannon et al. 2020; Deutsch et al. 2020a).

4. Discussion

4.1. The Smoothing of Topography by Ice

The statistically differentiable VRM^* populations within and outside of ISZs, combined with the reduced ruggedness within ISZs for at least nine of the 12 investigated craters, may be consistent with the presence of ice subduing surface topography.

Today, the distribution, physical form, and concentration of ice at the lunar poles are still poorly understood (e.g., Teodoro et al. 2014; Lawrence 2017), and these characteristics could influence surface texture. There are various optical remote sensing data that suggest that thin frosts or diffuse ice mixed with the regolith may be present at the surface (Zuber et al. 2012; Lucey et al. 2014; Hayne et al. 2015; Fisher et al. 2017; Li et al. 2018; Qiao et al. 2019), and previous work suggested that the presence of surface volatiles at the lunar poles is subduing surface roughness (Moon et al. 2020). Specifically, Moon et al. (2020) analyzed the surface roughness of Scott E crater derived from LROC NAC scattered-light images. A “brightness roughness” was calculated as the SD of the brightness gradient (DN m^{-1}) among neighboring pixels in the direction of steepest descent, representing changes in brightness

gradient over ~ 50 m (Moon et al. 2020). Moon et al. (2020) found that the brightness roughness in Scott E is lower in regions where surface ice is predicted to be thermally stable than it is in regions where either subsurface ice is predicted to be stable or no ice is predicted to be stable.

The 12 craters in our study population (Table 2) are located within the polar regions analyzed by Li et al. (2018) for the presence of diagnostic water-ice absorption features in Moon Mineralogy Mapper (M^3) data. Our study population includes both craters that do ($N = 7$) and do not ($N = 5$) host surface ice exposures, and Li et al. (2018) found that there was no bias in the acquisition of M^3 data for craters that lack detections of surface water ice. Because we observe a correlation between ISZs and smooth surface textures in both ice-bearing and ice-lacking craters, the surface ice detected using M^3 data is not expected to be the cause of the observed subdued topography.

Other remote sensing observations are also suggestive of surface frost at the lunar poles. Specifically, off-band/on-band UV albedo measured by the Ly α Mapping Project (LAMP; Hayne et al. 2015) and enhanced 1064 nm surface reflectance measured by the Lunar Orbiter Laser Altimeter (LOLA; Fisher et al. 2017; Qiao et al. 2019) are correlated with surface temperatures < 110 K. Unlike the ice exposures derived from M^3 data (Li et al. 2018), the anomalous LAMP spectral and LOLA reflectance characteristics are not unique to water ice, but their strong spatial correlation with ISZs is suggestive of water ice present at low abundances at the lunar surface

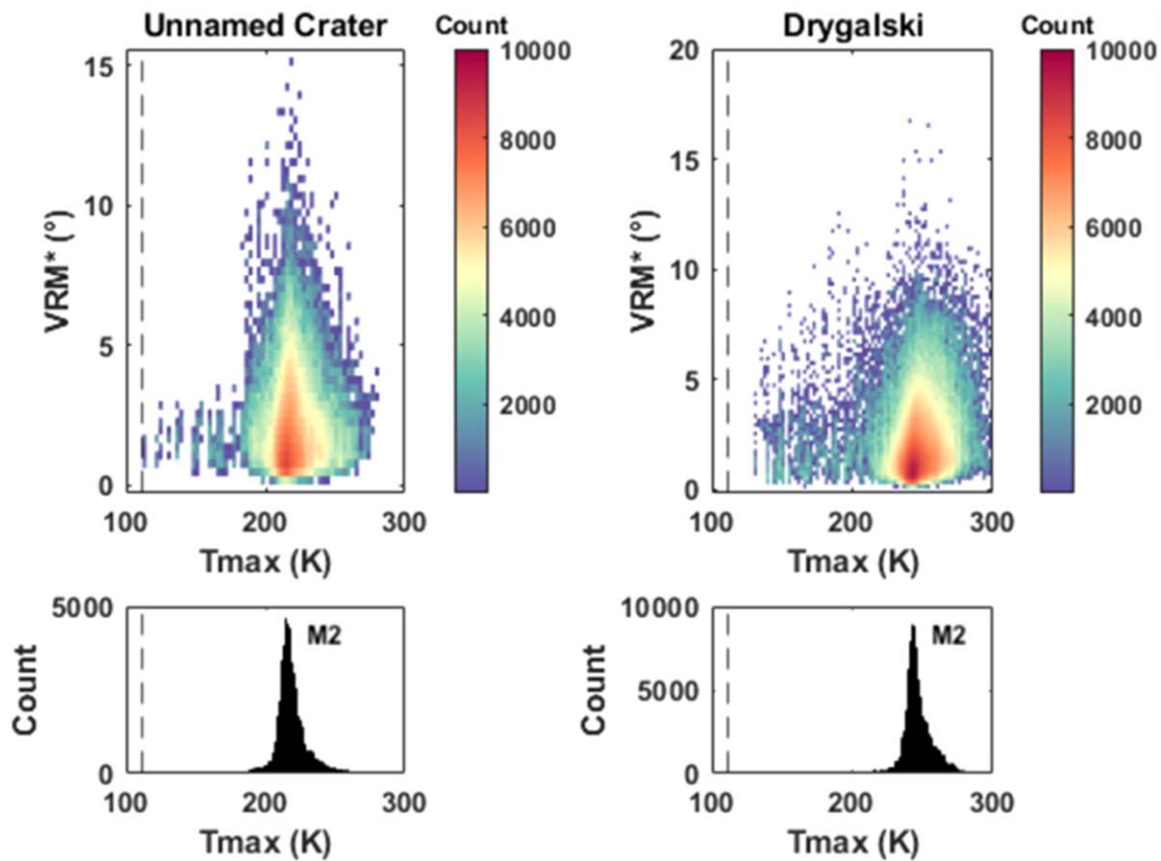


Figure 5. Binned scatter plots (with counts on a log scale) for VRM*s and maximum surface temperature of two polar craters that lack ISZs: an unnamed crater (84.9° N, 26.5°E) and Drygalski (79.6°S, 272.8°E). Texture indices were derived from DEMs with a pixel resolution of 120 m, and surface temperatures were upsampled to the same resolution using bilinear interpolation. $T_{\max} = 112$ K is marked with a dashed vertical line. Mode 1 is nonexistent, and Mode 2 is labeled.

(Zuber et al. 2012; Lucey et al. 2014; Hayne et al. 2015; Fisher et al. 2017; Qiao et al. 2019).

Just as it does with the M^3 ice detections (280 mpp; Li et al. 2018), our study population (Table 2) includes both craters that do and do not host the possible ice exposures identified in LAMP (250 mpp; Hayne et al. 2015) and LOLA (240 mpp; Fisher et al. 2017) data. The LAMP detections were limited in latitude to 82.5–90°S, and of the four craters in our study that are located in this range, Amundsen, the unnamed crater, and Wiechert have anomalous UV albedo consistent with water ice, while Idel’son L does not (Hayne et al. 2015). Anomalous high 1064 nm reflectance was observed in 11 of the 12 craters studied here (the exception being Lovelace), although we note that some of these 11 craters have only a couple of anomalous pixels (e.g., Idel’son L), while others have more substantial clusters of anomalous pixels (e.g., Cabeus B; Fisher et al. 2017). The observation of subdued surface textures in ISZs in craters without anomalous albedo (Hayne et al. 2015; Fisher et al. 2017) further suggests that the remotely sensed surface ice is not responsible for the low ruggedness values in ISZs.

In addition to surface frost, the lunar poles are likely to host subsurface ice, as inferred from neutron spectrometer data (Feldman et al. 2000, 2001; Lawrence et al. 2006; Elphic et al. 2007; Mitrofanov et al. 2010; Sanin et al. 2017; Starr et al. 2017), the LCROSS experiment (e.g., Colaprete et al. 2010; Luchsinger et al. 2021), and radiometer measurements (Yang et al. 2019). Measurements of polar crater morphometry indicate a shallowing of craters with latitude, suggestive of subsurface ice-rich deposits up to ~50 m thick (Kokhanov et al. 2015; Rubanenko et al. 2019),

and large volumes of subsurface ice are consistent with recent Monte Carlo modeling of ice deposition (Cannon et al. 2020). On Mars, the presence of subsurface ice has been correlated with subdued surface topography (Kreslavsky & Head 2000, 2002; Putzig et al. 2014), and it is possible that subsurface ice may also be responsible for the spatial correlation between low ruggedness indices and ISZs found here.

The typical difference between VRM*s inside and outside of ISZs is ~ 0.17 – 0.18 when using a 3×3 cell moving window on 120 mpp DEMs, and there are locations outside of ISZs that are just as smooth as locations within ISZs (Table 2; Figure 7). This finding is consistent with previous observations that suggest that ice does not exist at the lunar surface as thick, pervasive sheets (e.g., Haruyama et al. 2008; Fa & Cai 2013; Hayne et al. 2015; Fisher et al. 2017; Li et al. 2018; Mitchell et al. 2018; Farrell et al. 2019). While thin, frosty veneers (that drape but do not obscure the underlying regolith topography) may be present on the lunar surface (e.g., Zuber et al. 2012; Lucey et al. 2014; Hayne et al. 2015; Fisher et al. 2017; Li et al. 2018; Farrell et al. 2019; Qiao et al. 2019), micron- or millimeter-thick frosts are unlikely to affect the hectometer-scale ruggedness measured here. The presence of thick, ice-rich layers in the subsurface (Kokhanov et al. 2015; Rubanenko et al. 2019; Cannon et al. 2020; Luchsinger et al. 2021) may be more consistent with the subtle topography softening observed within ISZs at this scale. These observations may be similar to previous findings for Mars, where terrains appear smoother at short baselines, relating to a vertical difference of several

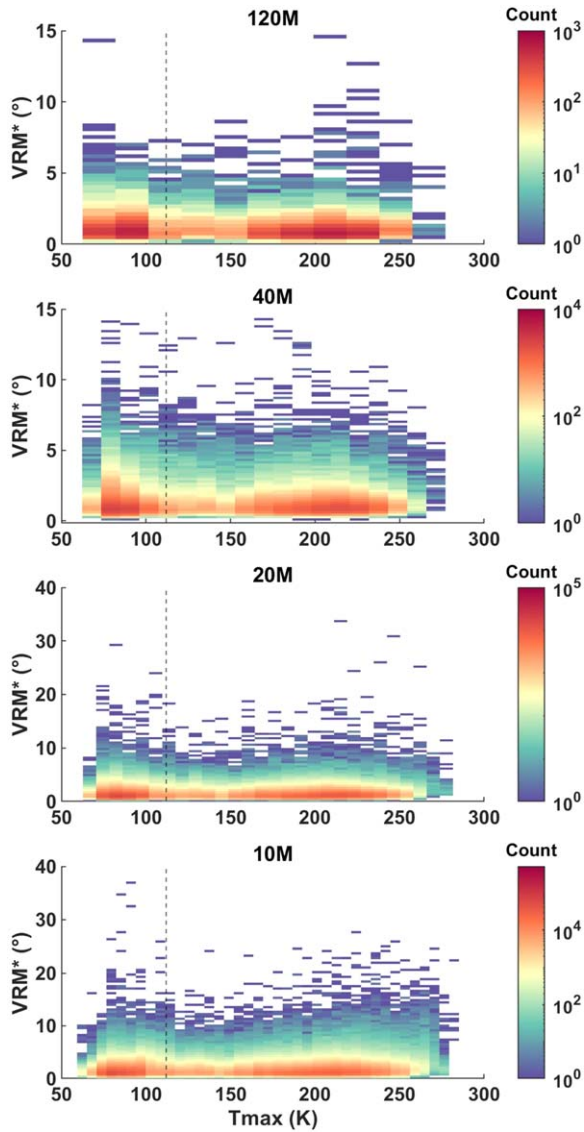


Figure 6. Binned scatter plots (with counts on a log scale) for VRM* and maximum surface temperature of an unnamed crater (88.6°S, 129°E), derived at pixel resolutions of 120, 40, 20, and 10 m. Surface temperatures were upsampled to the same resolution, and $T_{\max} = 112$ K is marked with a dashed vertical line. The same general patterns can be resolved at each spatial resolution.

meters, and may be related to the presence of seasonal frost or subsurface ices (Kreslavsky & Head 2000, 2002).

It is not clear why south polar craters Amundsen, Idel’son L, and Cabeus B show enhanced softening within their ISZs compared to other craters (Table 2). While Cabeus B ($\sim 0^\circ 34'$ of softening versus the typical $\sim 0^\circ 18'$) likely hosts some surface ice exposures as indicated by both M³ and LOLA data (Cabeus B is outside the range of the LAMP observations), Idel’son L and Amundsen may not. Idel’son L ($\sim 0^\circ 35'$ versus $\sim 0^\circ 18'$) does not host any ice exposures identified in either M³ or LAMP data, and it hosts only a single anomalously bright pixel identified in the LOLA observations (Hayne et al. 2015; Fisher et al. 2017; Li et al. 2018). Within Amundsen ($\sim 0^\circ 43'$ versus $\sim 0^\circ 18'$), anomalous albedo has been identified within LAMP and LOLA data, but M³ ice detections are notably lacking (Hayne et al. 2015; Fisher et al. 2017; Li et al. 2018). This again suggests that perhaps the smoothing within ISZs is not from surface ice exposures.

If the subdued ruggedness observed in ISZs is due to the presence of ice, then one possibility is that these two craters host greater amounts of subsurface ice than the other craters sampled, and the additional ice led to greater softening of the ISZ surface topography. There are multiple variables that affect how much ice has accumulated in any given crater, including the crater’s thermal environment (Paige et al. 2010; Siegler et al. 2016; Kloos et al. 2019) and age (Cannon et al. 2020; Deutsch et al. 2020a), as well as its exposure to ice accumulation and loss processes (Crider & Vondrak 2003; Hurley et al. 2012; Costello et al. 2020). As mentioned earlier, Amundsen, Idel’son L, and Cabeus B are not preferentially colder or older than other investigated craters (Tye et al. 2015; Williams et al. 2019; Cannon et al. 2020; Deutsch et al. 2020a). Perhaps it is possible that these craters were subject to relatively higher ice delivery rates and/or lower loss rates than the other sampled craters. Interestingly, these three craters are all located in the south polar region, and measurements of crater morphometry indicate that small south polar craters are generally shallower than small north polar craters. This has been suggested to be due to thicker icy layers at the lunar south pole (Kokhanov et al. 2015; Rubanenko et al. 2019). Cannon et al. (2020) suggested that this south–north disparity could be affected by small number statistics; if the majority of lunar ice was delivered by a few large, hydrated impacts, then more impacts in the southern hemisphere could lead to greater ice accumulation at the south pole.

We note that the present-day surface thermal environments of all of the craters in our study (Table 2) are amenable to the survival of surface water ice, including the craters that do not host M³-derived surface ice exposures (Li et al. 2018). However, thermal models suggest that surface ice would not have been stable in these exposure-lacking craters if the Moon was oriented at the paleo-axis predicted by Siegler et al. (2016). Subsurface ice, though, is predicted to have been stable in these craters under paleo-conditions, as well as today (Siegler et al. 2016; Li et al. 2018). If subsurface ice is indeed responsible for the low ruggedness indices that we measured with VRM*, then this ice is likely to be relatively ancient, given that the majority of ice accumulated at the lunar poles is predicted to have been deposited early on (e.g., Siegler et al. 2016; Cannon et al. 2020; Deutsch et al. 2020a).

4.2. Constraints on Subsurface Ice from Neutron Spectroscopy

If subsurface ice is indeed responsible for the clustering of low ruggedness values within some ISZs, then it must be abundant enough at some depth in order to affect the surface topography at the investigated spatial scales. One approach to constraining the abundance and depth of subsurface ice is with neutron spectroscopy (e.g., Lingenfelter et al. 1961; Feldman et al. 1991). Because hydrogen atoms have the same mass as neutrons, their presence causes neutrons to lose energy very efficiently. The Lunar Prospector Neutron Spectrometer (LPNS), with a penetration depth of ~ 1 m, measured decreases in the count rate of epithermal neutrons at the lunar poles, suggesting that there is an enhancement in the presence of hydrogen in the polar shallow subsurface (Feldman et al. 1998, 2000, 2001; Lawrence et al. 2006). When assuming that the hydrogen is in the form of water ice, the observed neutron suppression is consistent with models of 1.5 ± 0.8 wt. % water equivalent hydrogen (WEH) in the south polar region (Feldman et al. 2001), although the abundance in some local cold traps

Table 2

Statistics Reported on VRM*s Calculated for Regions inside ISZs ($T_{\max} \leq 112$ K) and outside ISZs ($T_{\max} > 112$ K), Including Mean, Standard Deviation (SD), and the 25th, 50th (Median), and 75th Percentiles

Crater Name (Location, Diameter)	Mean \pm SD		Percentiles (25th, 50th, 75th)	
	Inside ISZ	Outside ISZ	Inside ISZ	Outside ISZ
South Polar Region				
Amundsen (84.4°S, 83.1°E, 103.4 km)	1.45 \pm 1.11	1.88 \pm 1.36	(0.73, 1.10, 1.77)	(0.95, 1.47, 2.39)
Cabeus B* (82.3°S, 305.4, 59.6 km)	1.16 \pm 0.65	1.50 \pm 1.07	(0.72, 1.00, 1.42)	(0.79, 1.18, 1.86)
Hedervari (81.8°S, 85.6°E, 74.1 km)	1.33 \pm 0.83	1.59 \pm 1.02	(0.80, 1.16, 1.65)	(0.92, 1.32, 1.95)
Idel'son L (84.0°S, 118.6°E, 28.0 km)	1.66 \pm 1.28	2.01 \pm 1.37	(0.77, 1.30, 2.15)	(1.04, 1.61, 2.61)
Unnamed* (88.6°S, 129°E, 32.8 km)	1.32 \pm 0.88	1.18 \pm 0.83	(0.77, 1.09, 1.60)	(0.70, 0.98, 1.41)
Wichert (84.0°S, 164.7°E, 40.8 km)	1.27 \pm 0.91	1.34 \pm 0.90	(0.76, 1.04, 1.49)	(0.82, 1.14, 1.58)
North Polar Region				
Bosch (82.8°N, 133.6°E, 19.6 km)	2.54 \pm 1.35	2.36 \pm 1.32	(1.58, 2.24, 3.26)	(1.45, 2.04, 2.94)
Lovelace* (82.1°N, 250.0°E, 57.1 km)	1.21 \pm 0.92	1.22 \pm 0.93	(0.6, 0.95, 1.52)	(0.58, 0.93, 1.55)
Nansen F* (85.0°N, 62.6°E, 61.6 km)	2.27 \pm 1.42	2.34 \pm 1.44	(1.23, 1.90, 2.97)	(1.29, 1.99, 3.03)
Plaskett V* (82.2°N, 120.9°E, 49.1 km)	1.81 \pm 1.15	1.87 \pm 1.22	(1.06, 1.48, 2.20)	(1.05, 1.54, 2.33)
Rozhdestvenskiy U* (84.9°N, 151.9°E, 44.1 km)	1.39 \pm 0.85	1.49 \pm 0.93	(0.85, 1.20, 1.70)	(0.9, 1.27, 1.83)
Sylvester* (82.7°N, 278.3°E, 59.3 km)	1.55 \pm 1.12	1.68 \pm 1.08	(0.83, 1.24, 1.87)	(0.94, 1.41, 2.12)

Notes.

^a All values are derived from 120 mpp DEMs.

^b Craters that host surface water-ice exposures detected by Li et al. (2018) are denoted by an asterisk.

may be higher (Lawrence et al. 2006; Elphic et al. 2007; Eke et al. 2009; Teodoro et al. 2010).

We used the LPNS data to investigate the spatial correlation between modeled hydrogen content and the ISZs analyzed here. Time series neutron spectrometer data, specifically epithermal neutron count rate data used for mapping hydrogen variations, are publicly available online (<https://pds-geosciences.wustl.edu/missions/lunarp/index.htm>). These data can be subdivided into mission phases (Maurice et al. 2004), from which we extracted the low-altitude phase (average altitude of ~ 30 km). Using the spacecraft position and the 8 s epithermal neutron count rate data (8 s averages), we binned these samples in 5×5 km bins in polar stereographic projection as far as 600 km from each pole. Importantly, the binning of the LPNS data is much coarser (5000 mpp) than the spatial resolution of the measured surface texture (120 mpp). The binned data were then smoothed by two-dimensional convolution with Gaussian filters of different sizes, yielding multiple polar map layers of varying degrees of spatial smoothing. The size of filter kernels ranged from <10 to 160 km FWHM.

For Poisson-distributed epithermal neutron data, the number of counts accumulated in a given 5×5 km bin, N , is the signal, whereas the noise or uncertainty is \sqrt{N} . So the signal-to-noise ratio (S/N) is N/\sqrt{N} . The chosen value of filtered data for a given pixel was drawn from the corresponding pixel of the map layer for which the smallest-scale filter yielded an $S/N > 200$. In effect, this spatial filter convolution process “gathers” as many neutron counts as needed within a Gaussian-weighted area to provide an $S/N > 200$. In practice, this provides the smallest-scale smoothing for areas with high binned N (many revisits by Lunar Prospector) and progressively larger-scale

smoothing farther from the pole, where the LPNS sample density is lower.

Figure 11 shows the modeled hydrogen abundance for the 12 polar craters included in our analysis. South polar ISZs are relatively enhanced in modeled WEH in comparison to non-ISZs. The mean/median WEH is higher (or equal) inside ISZs than it is outside ISZs for each crater, except for the unnamed crater (Table 4). While the difference in modeled WEH is very small, it is greater than the SD for each population, except again for the unnamed crater. The investigated north polar craters do not uniformly exhibit a similar correlation between enhanced modeled WEH and ISZs (Figure 11).

Intriguingly, at both poles, the relative enhancement in WEH only occurs in ISZs that are smoother relative to their neighboring non-ISZs (Tables 2, 4). The only investigated south polar crater that does not have enhanced ISZ softening is the unnamed crater, and this is the only crater that does not have an enhancement in modeled WEH (Tables 2, 4). For the south polar craters whose ISZs are on average smoother than their non-ISZs, the modeled WEH abundance inside ISZs is higher than (for Amundsen, Cabeus B, Hedervari, and Wiechert) or equivalent to (Idel'son L) the modeled WEH abundance outside of ISZs. The correlation between relatively smooth ISZs and enhanced WEH is less clear in the north polar region. While Lovelace, Nansen F, Plaskett V, Rozhdestvenskiy U, and Sylvester all host ISZs that are comparatively smoother than their non-ISZs (Table 2), only Lovelace, Nansen F, and Rozhdestvenskiy U host ISZs that are enhanced in modeled WEH in comparison to their non-ISZs (Table 4). We again note the statistical noise associated with VRM* values in ISZ and non-ISZ populations; there is substantial overlap in VRM*s inside and outside ISZs, and the difference in mean/median VRM*s is typically less than the SD. It is also

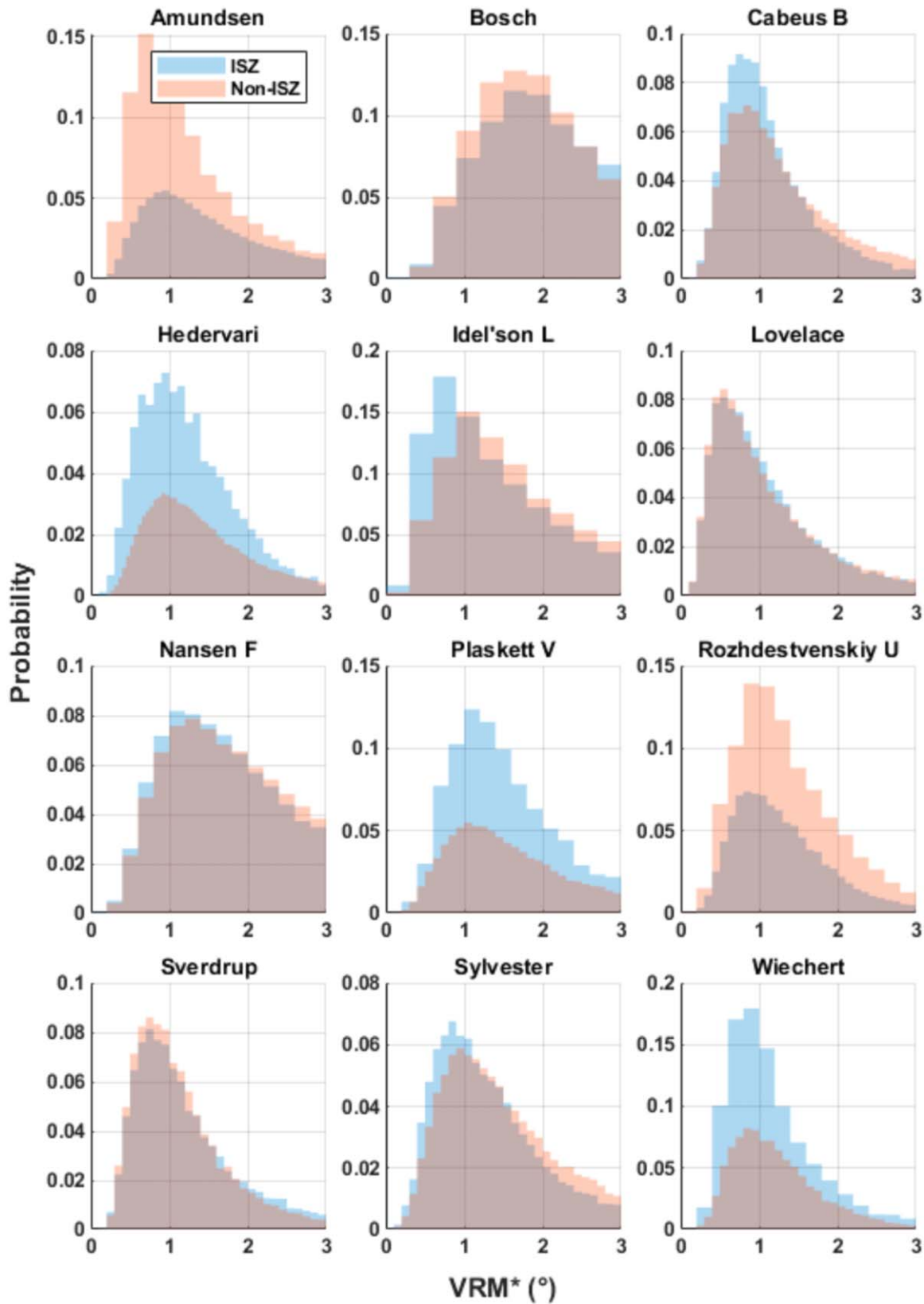


Figure 7. Distribution of VRM*'s within ISZs (blue) and outside ISZs (pink) for each crater.

important to appreciate the large spatial footprint of the LPNS data and thus the derived H models.

Overall, the presented models of hydrogen content suggest that there is more H present beneath the ISZs than there is

beneath the non-ISZs for at least four of the six investigated south polar craters, and all four of these craters show relative softening as measured by VRM*'s. These models also suggest that there is more H present beneath the ISZs for three of the six

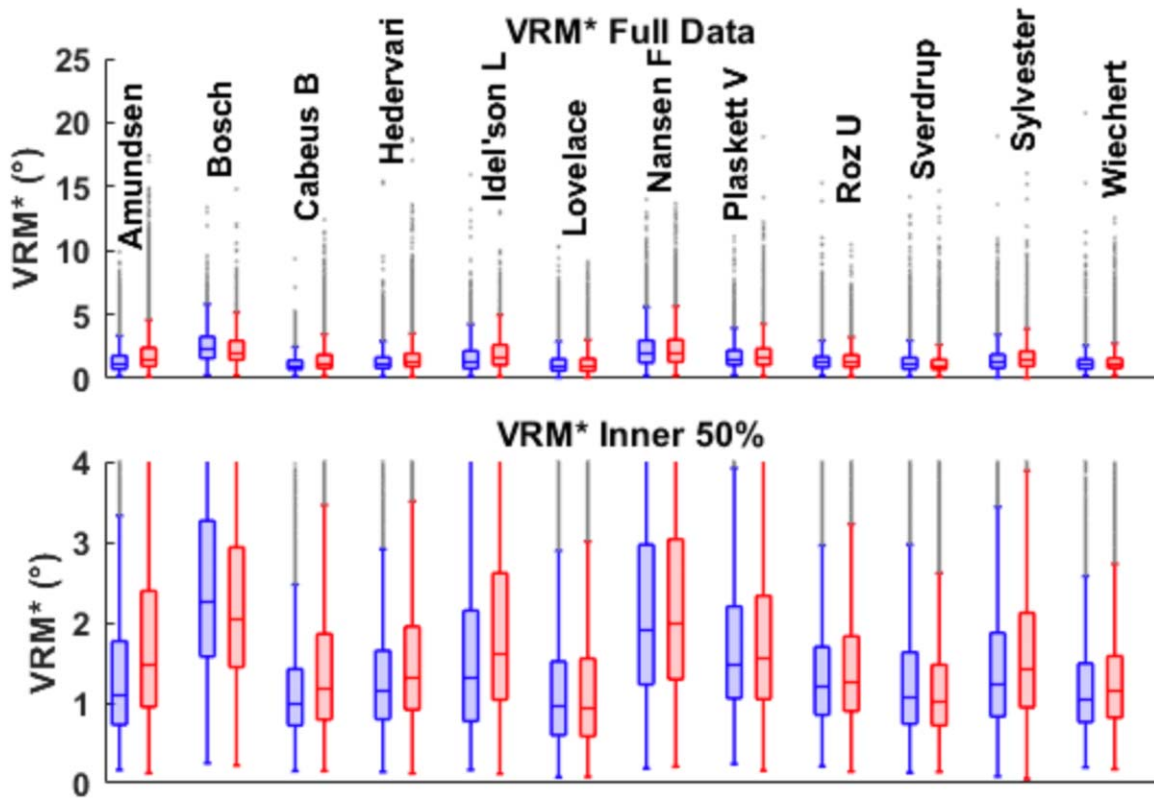


Figure 8. Box plots show the distribution of VRM*s within ISZs (blue) and outside ISZs (red) for each crater. The boxes denote the inner 50% of data, where the median is denoted by a horizontal line dividing each box. Statistical outliers are denoted by gray dots.

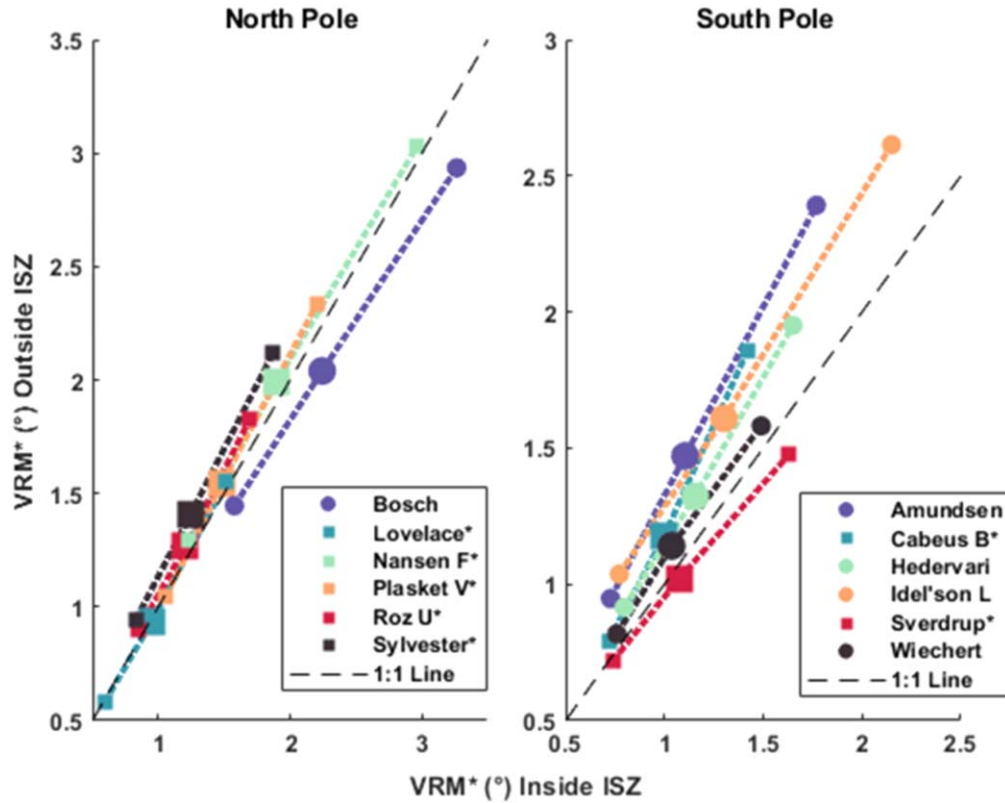


Figure 9. Comparison of VRM* values inside (x-axis) and outside (y-axis) ISZs for each crater. Craters that have relatively smoother ISZs in comparison to non-ISZs plot above the black dashed 1:1 line. Each crater is represented by a dashed line connecting its 25th, 50th (median), and 75th percentile values. Craters that host surface water-ice exposures detected by Li et al. (2018) are denoted by an asterisk and plotted as a square.

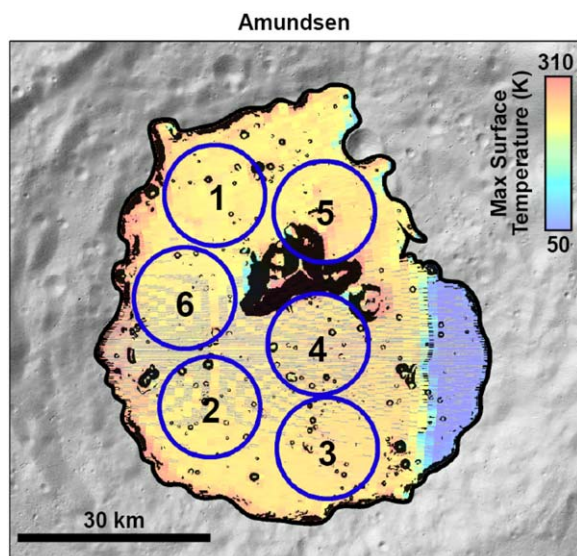


Figure 10. Locations of six adjacent regions (blue circles) outside of Amundsen’s ISZ. Each circular region has a surface area of $\sim 200 \text{ km}^2$. Slopes $< 10^\circ$ are masked in black. Maximum surface temperature (Williams et al. 2019) within Amundsen’s study area is shown on top of a LOLA hillshade map.

Table 3

Median VRM^as Calculated for Small Regions (Figure 10) outside of Amundsen’s ISZ and Compared to the Median VRM^a Inside Amundsen’s ISZ

Amundsen Study Area	Median VRM ^a (deg)
Polygon 1	1.82
Polygon 2	2.27
Polygon 3	2.00
Polygon 4	2.58
Polygon 5	1.80
Polygon 6	1.80
Inside ISZ	1.10

Notes.

^a All values are derived from 120 mpp DEMs.

investigated north polar craters, and all three of these ISZs also show relative softening. The low abundances of H implied by these hydrogen models are not expected to be enough to soften the overlying topography at the investigated spatial scale. If ice is the source of the observed softened topography, then perhaps it is more concentrated at a depth deeper than what is sensed by the LPNS ($\sim 1 \text{ m}$). Importantly, these low abundances are model dependent, and local variations (and thus enhancements) in ice content and distribution are expected to be present (e.g., Lawrence et al. 2006; Elphic et al. 2007; Eke et al. 2009; Teodoro et al. 2010).

The lack of enhanced neutron suppression at specific craters does not necessarily mean that ice is absent in the subsurface, as ice could be present at undetectably low concentrations or be buried at deeper depths. Impact gardening models suggest that surface ice would be gardened to a depth of 1 m in $< 1 \text{ Gyr}$ by icy secondary impactors, or in $< 100 \text{ Myr}$ by rocky secondaries (Costello et al. 2020). Thus, given that much of the lunar polar

ice is expected to be relatively ancient (e.g., Siegler et al. 2016; Lawrence 2017; Cannon et al. 2020; Costello et al. 2020; Deutsch et al. 2020a), it has likely been gardened to below 1 m. The process of regolith gardening from impact bombardment affects the durability of volatiles as a sustainable resource for exploration, as gardening drives modifications in volatile distribution and abundance (Crider & Vondrak 2003; Hurley et al. 2012; Benna et al. 2019; Costello et al. 2020). Measuring the physical texture of polar ISZs could help inform future surface evolution models as we try to understand the modification of polar craters and their ice inventories.

4.3. Signals of Subdued Topography in Mini-RF Data

Radar measurements, which penetrate below the surface, can also help characterize the presence of thick water-ice deposits owing to the distinctive radar polarization difference between ice and silicate regolith (e.g., Hapke 1990). While radar observations have helped in this way to study ice deposits on other terrestrial bodies, including Mercury (e.g., Slade et al. 1992; Harmon et al. 2011; Chabot et al. 2018) and Mars (e.g., Muhleman et al. 1991; Harmon & Nolan 2017), lunar radar experiments have been less conclusive. Earth-based radar observations of the Moon do not show evidence for concentrated water-ice deposits (Stacy et al. 1997; Campbell et al. 2006), and spacecraft radar observations are suggestive of only patches of ice (Spudis et al. 2010; Thomson et al. 2012). The Mini-RF instrument currently orbiting the Moon measures wavelength-scale surface roughness and was intended to help identify water-ice deposits (Nozette et al. 2010; Patterson et al. 2017, 2020). However, radar observations are complicated by their sensitivity to the presence of rocky materials, and previous studies have demonstrated a correlation between enhanced circular polarization ratios (CPRs) and less mature regolith (e.g., Thomson et al. 2012; Fa & Cai 2013; Fa & Eke 2018). For example, Thomson et al. (2012) found that the Mini-RF measurements of Shackleton crater are consistent with the downslope movement of material causing enhanced decimeter-scale surface roughness, rather than the presence of ice.

We used the monostatic, geodetically controlled polar mosaics presented by Jozwiak et al. (2019) to study the correlation between surface temperature and CPR in each of our 12 craters. We found that each crater’s CPR is not systematically enhanced where average or maximum surface temperatures are $\leq 112 \text{ K}$. Conversely, we found that the radar signal is typically slightly subdued in these ISZs (Table 5). The mean/median CPR inside ISZs is lower than it is outside ISZs for nine of the 12 analyzed craters, the exceptions being Amundsen, Idel’son L, and Rozhdestvenskiy U (Table 5). Interestingly, Amundsen and Idel’son L are two craters that show the greatest softening in their ISZs (Table 2).

But again, the ISZ and non-ISZ CPR populations are nearly overlapped, and the SD is usually higher than the differences in mean/median CPRs (Table 5). The general patterns observed in CPR- T_{max} space (e.g., Figure 12) may suggest that the Mini-RF signal is more indicative of surface roughness than of water-ice deposits at these sites, consistent with the finding that enhanced CPR inside anomalous polar craters is likely to be due to the presence of rocks instead of ice (Fa & Cai 2013; Fa & Eke 2018). However, we found that CPRs and our VRM^as are not statistically linearly correlated (Table 5). Overall, additional surface experiments (including radar) are needed at the lunar poles to fully understand the presence of subsurface ice.

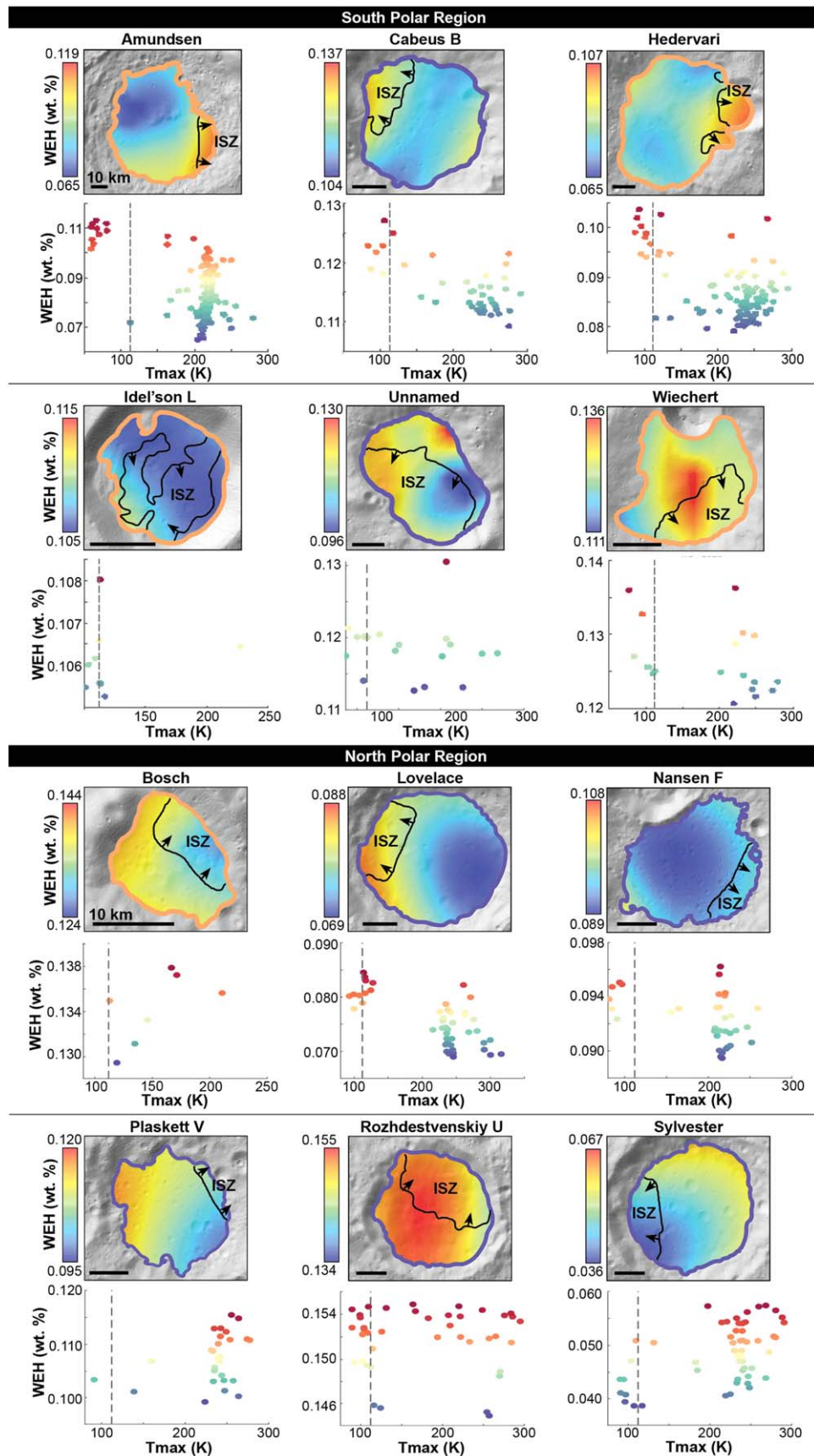


Figure 11. Inferred WEH abundance within each analyzed crater, with ISZs marked by black contours. Each scale bar in the lower left map corner denotes a distance of 10 km. Scatter plots show the relationship between modeled WEH and maximum surface temperature. $T_{\max} = 112$ K is marked with a dashed vertical line. Temperatures were down-sampled to the spatial resolution of the neutron data (5000 mpp).

Table 4

Statistics Reported on WEH Abundance (wt. %) for Regions inside ISZs ($T_{\max} \leq 112$ K) and outside ISZs ($T_{\max} > 112$ K) for 5000 mpp Data, Including Mean, Standard Deviation (SD), and the 25th, 50th (Median), and 75th Percentiles

Location Crater	Mean \pm SD		Percentiles (25th, 50th, 75th)	
	Inside ISZ	Outside ISZ	Inside ISZ	Outside ISZ
South Polar Region				
Amundsen	0.109 ± 0.001	0.085 ± 0.003	(0.084, 0.109, 0.110)	(0.075, 0.082, 0.092)
Cabeus B*	0.123 ± 0.0004	0.115 ± 0.001	(0.119, 0.123, 0.123)	(0.112, 0.114, 0.116)
Hedervari	0.099 ± 0.0002	0.088 ± 0.002	(0.000, 0.098, 0.099)	(0.083, 0.086, 0.088)
Idel'son L	0.106 ± 0.0003	0.106 ± 0.0006	(0.105, 0.106, 0.107)	(0.106, 0.106, 0.106)
Unnamed*	0.111 ± 0.002	0.113 ± 0.004	(0.104, 0.111, 0.117)	(0.112, 0.115, 0.119)
Wiechert	0.129 ± 0.001	0.126 ± 0.004	(0.126, 0.127, 0.133)	(0.123, 0.125, 0.129)
North Polar Region				
Bosch	0.130 ± 0.001	0.134 ± 0.0004	(0.129, 0.13, 0.131)	(0.131, 0.133, 0.136)
Lovelace*	0.079 ± 0.0001	0.076 ± 0.001	(0.079, 0.079, 0.08)	(0.071, 0.074, 0.079)
Nansen F*	0.093 ± 0.0003	0.092 ± 0.001	(0.093, 0.093, 0.095)	(0.09, 0.091, 0.093)
Plaskett V*	0.103 ± 0.000	0.107 ± 0.001	(0.103, 0.103, 0.103)	(0.103, 0.107, 0.112)
Rozhdestvenskiy U*	0.152 ± 0.0003	0.151 ± 0.0003	(0.150, 0.153, 0.153)	(0.149, 0.152, 0.154)
Sylvester*	0.042 ± 0.002	0.049 ± 0.002	(0.039, 0.042, 0.045)	(0.046, 0.049, 0.054)

Notes.

^a Craters that host surface water-ice exposures detected by Li et al. (2018) are denoted by an asterisk.

Table 5

Statistics Reported on CPR from East-looking Mini-RF data (Jozwiak et al. 2019) for Regions inside ISZs ($T_{\max} \leq 112$ K) and outside ISZs ($T_{\max} > 112$ K), Including Mean, Standard Deviation (SD), the 25th, 50th (Median), and 75th Percentiles, and the Correlation Coefficient between CPRs and VRM*s

Location Crater	Mean \pm SD		Percentiles (25th, 50th, 75th)		CC	
	Inside ISZ	Outside ISZ	Inside ISZ	Outside ISZ	Inside ISZ	Outside ISZ
South Polar Region						
Amundsen	0.517 ± 0.13	0.508 ± 0.127	(0.430, 0.490, 0.580)	(0.420, 0.480, 0.570)	0.312	0.308
Cabeus B*	0.296 ± 0.078	0.383 ± 0.112	(0.240, 0.280, 0.330)	(0.300, 0.360, 0.440)	-0.059	0.213
Hedervari	0.512 ± 0.106	0.541 ± 0.112	(0.440, 0.500, 0.570)	(0.460, 0.530, 0.600)	0.158	0.142
Idel'son L	0.583 ± 0.116	0.561 ± 0.102	(0.510, 0.560, 0.640)	(0.490, 0.550, 0.620)	0.285	0.207
Unnamed*	0.350 ± 0.099	0.446 ± 0.222	(0.290, 0.330, 0.380)	(0.300, 0.380, 0.530)	0.401	0.178
Wiechert	0.366 ± 0.093	0.361 ± 0.092	(0.300, 0.350, 0.400)	(0.300, 0.340, 0.400)	0.170	0.137
North Polar Region						
Bosch	0.366 ± 0.093	0.361 ± 0.092	(0.300, 0.350, 0.400)	(0.300, 0.340, 0.400)	0.323	0.381
Lovelace*	0.483 ± 0.114	0.490 ± 0.103	(0.410, 0.460, 0.530)	(0.420, 0.470, 0.540)	0.267	0.265
Nansen F*	0.431 ± 0.115	0.420 ± 0.106	(0.350, 0.410, 0.490)	(0.350, 0.400, 0.470)	0.280	0.272
Plaskett V*	0.403 ± 0.121	0.396 ± 0.125	(0.320, 0.380, 0.470)	(0.310, 0.380, 0.460)	0.138	0.235
Rozhdestvenskiy U*	0.393 ± 0.098	0.377 ± 0.077	(0.330, 0.370, 0.430)	(0.320, 0.370, 0.420)	0.200	0.153
Sylvester*	0.461 ± 0.135	0.465 ± 0.118	(0.370, 0.430, 0.520)	(0.390, 0.450, 0.520)	0.246	0.250

Notes.

^a Craters that host surface water-ice exposures detected by Li et al. (2018) are denoted by an asterisk.

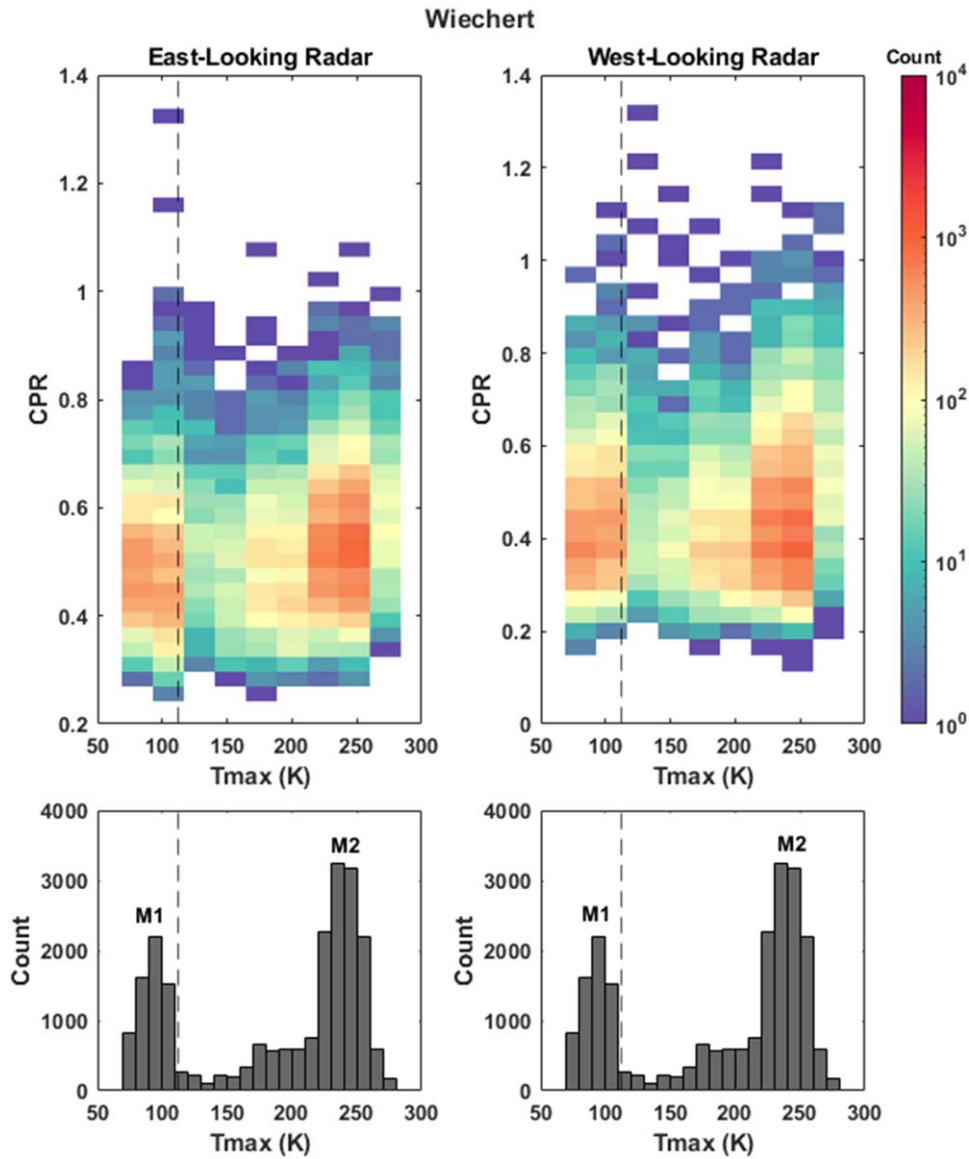


Figure 12. Binned scatter plots (with counts on a log scale) for CPRs and maximum surface temperature of Lovelace at a pixel resolution of 120 m. Radar data are from Jozwiak et al. (2019) and include both (a) east-looking (0° – 180°) and (b) west-looking (180° – 360°) radar, providing subtle differences in the coverage. Modes 1 and 2 are labeled, and $T_{\max} = 112$ K is marked with the dashed vertical line.

We also note that textural changes unrelated to the presence of ice can occur in cold polar regolith. For example, experiments using lunar simulant suggest that thermal cycling can compact the upper lunar regolith (Chen et al. 2006; Hapke 1990; Metzger et al. 2018). Thus, in the coldest portions of the poles (i.e., ISZs), where the thermal wave amplitude is smaller, the upper soil is predicted to be effectively “looser” (Metzger et al. 2018). This prediction is consistent with infrared emissions measured by the Diviner radiometer that suggest that the soil is looser where insolation is lower (Hayne et al. 2015, 2017). Additionally, the timing of the near-infrared flash that followed the LCROSS impact has also been interpreted as a possible indicator of fluffier regolith in PSRs (Schultz et al. 2010). Looser regolith unlikely influences surface texture at the scales measured here, but a complete framework of processes that influence surface texture of ISZs should consider those operating at the grain-size scale too.

5. Conclusions

We measured surface ruggedness using VRM*s in 12 polar craters on the Moon. These craters have a bimodal distribution in maximum surface temperatures. Mode 1 is located at low surface temperatures where T_{\max} is ≤ 112 K, the temperature at which water ice is stable against sublimation at the surface over geologic timescales (Vasavada et al. 1999; Paige et al. 2010). Mode 2 is much broader, it occurs at higher temperatures, and its location varies depending on the individual thermal environment of any given crater.

Constraining the locations and environments of anomalous surface textures (i.e., smoothing) may provide insight into the locations of ice. For nine of the 12 craters we investigated, the mean surface ruggedness is lower (i.e., smoother) inside ISZs than it is outside of ISZs, and it may be consistent with the presence of volatiles softening the polar topography. The smoothing of ISZs occurs in both craters that do and do not have putative surface ice exposures (Hayne et al. 2015; Fisher et al. 2017; Li et al. 2018),

and thus we favor the possibility that subsurface ice, rather than surface ice, may be responsible for the smoothing of ISZs. The softened ISZs also tend to be correlated with slightly enhanced WEH abundances (especially for south polar craters), although the estimated low H abundances modeled for the upper meter of polar regolith are unlikely to account for all of the smoothing measured at this hectometer scale, derived from 120 mpp DEMs.

Today, the relationship between surface and subsurface ice is not clear. The variation between individual craters in the inferred amount of surface ice (Zuber et al. 2012; Lucey et al. 2014; Hayne et al. 2015; Fisher et al. 2017; Li et al. 2018; Qiao et al. 2019), subsurface ice (e.g., Feldman et al. 2000, 2001; Lawrence et al. 2006; Elphic et al. 2007; Mitrofanov et al. 2010; Boynton et al. 2012; Sanin et al. 2017; Starr et al. 2017), and smooth textures (here) highlights the heterogeneous nature of ice at the lunar poles. Understanding the scales and drivers of this variability is an important step in studying the processes that deliver, modify, and destroy lunar volatiles over time. Future exploration of polar craters, especially applying ground-based remote sensing and drilling (e.g., Colaprete et al. 2020), is essential in resolving the presence, form, and abundance of surface and/or near-surface volatiles that may be altering the surface topography.

We gratefully acknowledge the helpful reviews of Dr. Le Qiao and an anonymous reviewer in improving our manuscript. A.N.D. was supported by an appointment to the NASA Postdoctoral Program at Ames Research Center, administered by Universities Space Research Association under contract with NASA.

Supporting Data

Archived data products are available at Zenodo: doi:[10.5281/zenodo.4716357](https://doi.org/10.5281/zenodo.4716357).

ORCID iDs

Ariel N. Deutsch  <https://orcid.org/0000-0001-9831-3619>

References

- Amatulli, G., Domisch, S., Tuanmu, M.-N., et al. 2018, *NatSD*, **5**, 180040
 Arnold, J. R. 1979, *JGR*, **84**, 5659
 Barker, M. K., Mazarico, E., Neumann, G. A., et al. 2020, *P&SS*, **203**, 105119
 Benna, M., Hurley, D. M., Stubbs, T. J., Mahaffy, P. R., & Elphic, R. C. 2019, *NatGe*, **12**, 333
 Boynton, W. V., Droege, G. F., Mitrofanov, I. G., et al. 2012, *JGRE*, **117**, E00H33
 Campbell, D. B., Campbell, B. A., Carter, L. M., Margot, J.-L., & Stacy, N. J. S. 2006, *Natur*, **443**, 835
 Cannon, K. M., Deutsch, A. N., Head, J. W., & Britt, D. T. 2020, *GeoRL*, **47**, e88920
 Chabot, N. L., Shread, E. E., & Harmon, J. K. 2018, *JGRE*, **123**, 666
 Chen, K., Cole, J., Conger, C., et al. 2006, *Natur*, **442**, 257
 Colaprete, A., Elphic, R. C., Shirley, M., et al. 2020, *LPSC*, **51**, 2241
 Colaprete, A., Schultz, P., Heldmann, J., et al. 2010, *Sci*, **330**, 463
 Costello, E. S., Ghent, R. R., Hirabayashi, M., & Lucey, P. G. 2020, *JGRE*, **125**, e06172
 Crider, D. H., & Vondrak, R. R. 2003, *JGRE*, **108**, 5079
 De Rosa, D., Bussey, B., Cahill, J. T., et al. 2012, *P&SS*, **74**, 224
 Deutsch, A. N., Head, J. W., & Neumann, G. A. 2020a, *Icar*, **336**, 113455
 Deutsch, A. N., Head, J. W., Neumann, G. A., Kreslavsky, M. A., & Barker, M. K. 2020b, *GeoRL*, **47**, e87782
 Eke, V. R., Teodoro, L. F. A., & Elphic, R. C. 2009, *Icar*, **200**, 12
 Elphic, R. C., Eke, V. R., Teodoro, L. F. A., Lawrence, D. J., & Bussey, D. B. J. 2007, *GeoRL*, **34**, L13204
 Fa, W., & Cai, Y. 2013, *JGRE*, **118**, 1582
 Fa, W., & Eke, V. R. 2018, *JGRE*, **123**, 2119
 Farrell, W. M., Hurley, D. M., Poston, M. J., et al. 2019, *GeoRL*, **46**, 8680
 Feldman, W. C., Lawrence, D. J., Elphic, R. C., et al. 2000, *JGRE*, **105**, 4175
 Feldman, W. C., Maurice, S., Binder, A. B., et al. 1998, *Sci*, **281**, 1496
 Feldman, W. C., Maurice, S., Lawrence, D. J., et al. 2001, *JGRE*, **106**, 23231
 Feldman, W. C., Reedy, R. C., & McKay, D. S. 1991, *GeoRL*, **18**, 2157
 Fisher, E. A., Lucey, P. G., Lemelin, M., et al. 2017, *Icar*, **292**, 74
 Hapke, B. 1990, *Icar*, **88**, 407
 Harmon, J. K., & Nolan, M. C. 2017, *Icar*, **281**, 162
 Harmon, J. K., Slade, M. A., & Rice, M. S. 2011, *Icar*, **211**, 37
 Haruyama, J., Ohtake, M., Matsunaga, T., et al. 2008, *Sci*, **322**, 938
 Hayne, P. O., Aharonson, O., & Schorghofer, N. 2020, *NatAs*, **5**, 169
 Hayne, P. O., Bandfield, J. L., Siegler, M. A., et al. 2017, *JGRE*, **122**, 2371
 Hayne, P. O., Hendrix, A., Sefton-Nash, E., et al. 2015, *Icar*, **255**, 58
 Heldmann, J. L., Colaprete, A., Elphic, R. C., et al. 2016, *AcAau*, **127**, 308
 Hobson, R. D. 1972, in *Spatial Analysis in Geomorphology*, ed. R. J. Chorley (New York: Harper and Row), 221
 Hurley, D. M., Lawrence, D. J., Bussey, D. B. J., et al. 2012, *GeoRL*, **39**, L09203
 Ivanov, M. A., Hiesinger, H., Abdrakhimov, A. M., et al. 2015, *P&SS*, **117**, 45
 Jawin, E. R., Kiefer, W. S., Fasset, C. I., et al. 2014, *JGRE*, **119**, 2331
 Jozwiak, L. M., Patterson, G. W., Perkins, R., & the Mini-RF team 2019, EPSC-DPS Joint Meeting, **13**, 754
 Kloos, J. L., Moores, J. E., Sangha, J., Nguyen, T. G., & Schorghofer, N. 2019, *JGRE*, **124**, 1935
 Kokhanov, A. A., Kreslavsky, M. A., & Karachevtseva, I. P. 2015, *SoSyR*, **49**, 295
 Kreslavsky, M. A., & Head, J. W. 2002, *GeoRL*, **29**, 1719
 Kreslavsky, M. A., Head, J. W., Neumann, G. A., et al. 2013, *Icar*, **226**, 52
 Kreslavsky, Mikhail A., & Head, J. W. 2000, *JGR*, **105**, 26695
 Lawrence, D. J. 2017, *JGRE*, **122**, 21
 Lawrence, D. J., Feldman, W. C., Elphic, R. C., et al. 2006, *JGRE*, **111**, E08001
 Li, S., Lucey, P. G., Milliken, R. E., et al. 2018, *PNAS*, **115**, 8907
 Lingenfelter, R. E., Canfield, E. H., & Hess, W. N. 1961, *JGR*, **66**, 2665
 Lucey, P. G., Neumann, G. A., Riner, M. A., et al. 2014, *JGRE*, **119**, 1665
 Luchsinger, K. M., Chanover, N. J., & Strycker, P. D. 2021, *Icar*, **354**, 114089
 Maurice, S., Lawrence, D. J., Feldman, W. C., Elphic, R. C., & Gasnault, O. 2004, *JGRE*, **109**, E07S04
 Mazarico, E., Neumann, G. A., Smith, D. E., Zuber, M. T., & Torrence, M. H. 2011, *Icar*, **211**, 1066
 Metzger, P. T., Anderson, S., & Colaprete, A. 2018, in 16th Biennial International Conf. on Engineering, Science, Construction, and Operations in Challenging Environments (Reston, VA: American Society of Civil Engineers), 79
 Mitchell, J., Lawrence, S., Robinson, M., Speyerer, E., & Denevi, B. 2018, *P&SS*, **162**, 133
 Mitrofanov, I. G., Sanin, A. B., Boynton, W. V., et al. 2010, *Sci*, **330**, 483
 Moon, S., Paige, D. A., Siegler, M. A., & Russell, P. S. 2020, *GeoRL*, **48**, e90780
 Muhleman, D. O., Butler, B. J., Grossman, A. W., & Slade, M. A. 1991, *Sci*, **253**, 1508
 Neumann, G. A., Glaeser, P. A., Hiesinger, H., Zuber, M. T., & Smith, D. E. 2015, *LPSC*, **46**, 2218
 Nozette, S., Spudis, P., Bussey, B., et al. 2010, *SSRv*, **150**, 285
 Ohtake, M., Karouji, Y., Inoue, H., et al. 2020, *LPSC*, **51**, 1830
 Paige, D. A., Siegler, M. A., Zhang, J. A., et al. 2010, *Sci*, **330**, 479
 Patterson, G. W., Jozwiak, L. M., Leeburn, J. M., et al. 2020, *LPICo*, **2241**, 5158
 Patterson, G. W., Stickley, A. M., Turner, F. S., et al. 2017, *Icar*, **283**, 2
 Putzig, N. E., Phillips, R. J., Campbell, B. A., et al. 2014, *JGRE*, **119**, 1936
 Qiao, L., Ling, Z., Head, J. W., Ivanov, M. A., & Liu, B. 2019, *E&SS*, **6**, 467
 Rosenburg, M. A., Aharonson, O., Head, J. W., et al. 2011, *JGRE*, **116**, E02001
 Rubanenko, L., Venkatraman, J., & Paige, D. A. 2019, *NatGe*, **12**, 597
 Sanin, A. B., Mitrofanov, I. G., Litvak, M. L., et al. 2017, *Icar*, **283**, 20
 Sappington, J. M., Longshore, K. M., & Thompson, D. B. 2007, *Journal of Wildlife Management*, **71**, 1419
 Schorghofer, N., & Aharonson, O. 2014, *ApJ*, **788**, 169
 Schultz, P. H., Hermalyn, B., Colaprete, A., et al. 2010, *Sci*, **330**, 468
 Siegler, M. A., Miller, R. S., Keane, J. T., et al. 2016, *Natur*, **531**, 480
 Slade, M. A., Butler, B. J., & Muhleman, D. O. 1992, *Sci*, **258**, 635
 Spudis, P. D., Bussey, D. B. J., Baloga, S. M., et al. 2010, *GeoRL*, **37**, L06204
 Stacy, N. J. S., Campbell, D. B., & Ford, P. G. 1997, *Sci*, **276**, 1527
 Starr, R. D., Litvak, M. L., Petro, N. E., et al. 2017, *P&SS*, **162**, 105

- Teodoro, L. F. A., Eke, V. R., & Elphic, R. C. 2010, [GeoRL](#), **37**, L12201
- Teodoro, L. F. A., Eke, V. R., Elphic, R. C., Feldman, W. C., & Lawrence, D. J. 2014, [JGRE](#), **119**, 574
- Thomson, B. J., Bussey, D. B. J., Neish, C. D., et al. 2012, [GeoRL](#), **39**, L14201
- Tye, A. R., Fassett, C. I., Head, J. W., et al. 2015, [Icar](#), **255**, 70
- Vasavada, A. R., Paige, D. A., & Wood, S. E. 1999, [Icar](#), **141**, 179
- Wang, J., Kreslavsky, M. A., Liu, J., et al. 2020, [JGRE](#), **125**, e06091
- Watson, K., Murray, B., & Brown, H. 1961, [JGR](#), **66**, 1598
- Williams, J.-P., Greenhagen, B. T., Paige, D. A., et al. 2019, [JGRE](#), **124**, 2505
- Yang, F., Xu, Y., Chan, K. L., Zhang, X., Hu, G., & Li, Y. 2019, [AdAst](#), 2019, 3940837
- Zuber, M. T., Head, J. W., Smith, D. E., et al. 2012, [Natur](#), **486**, 378